Reviews of Electromagnetics, Vol. V, 2026
EuCAP 2026 Special Issue
DOI: 10.53792/RoE/2026/26008

Reviews of Electromagnetics
EuCAP 2026 Special Issue

Design and Optimization of a Broadband Meander-Line Polarizer with Cylindrical-Aperture Integration

Alp Emir Gürsoy[1,2]*, Mustafa Kuloğlu[1], Kamil Karaçuha[2]

Abstract
This paper presents a semi-analytical design framework for broadband, conformal, multilayer linear-to-circular polarization converters. Each printed meander-line sheet is represented by a frequency-dependent tensor admittance retrieved from periodic full-wave unit-cell simulations, while the intervening dielectric and spacer regions are modeled using cascaded 4×4 transmission (ABCD) matrices. A hybrid optimization procedure combining a genetic algorithm with gradient-based local refinement is used to synthesize multilayer configurations subject to axial-ratio and transmission constraints over a broad frequency range. The formulation is first validated against full-wave simulations using a five-layer test polarizer. A separately optimized five-layer polarizer is then conformed to and integrated with the cylindrical aperture of a test horn antenna. The integrated configuration provides a 3-dB axial-ratio bandwidth of 66.6% over 10–20 GHz, with a maximum insertion loss of 0.55 dB. The conformal implementation preserves the principal radiation patterns and provides stable polarization conversion over the antenna main beam, demonstrating the suitability of the proposed framework for broadband aperture-integrated polarization conversion.

Key terms
Circular polarization; Transmission-line model; Conformal surface; Broadband polarizer; Meander lines; Metasurfaces; Cascaded structures

[1] *REHİS, ASELSAN, Ankara, Türkiye*
[2] *Department of Electronics and Communication Engineering, İTÜ, İstanbul, Türkiye*
*__Corresponding author__: aemirgursoy@aselsan.com

Received: 19/06/2026, Accepted: 20/10/2026, Published: 12/11/2026

1. Introduction

Circularly polarized (CP) antennas are used in satellite communications, global navigation satellite systems, radar, and electronic warfare [1, 2]. Compared with linear polarization, circular polarization is insensitive to the polarization-angle rotation produced by Faraday rotation [3]; it also provides a fixed 3-dB polarization-mismatch loss when receiving a linearly polarized signal of unknown orientation, which is useful in direction-finding applications [4]. Consequently, planar spiral and four-arm sinuous antennas are common choices for broadband direction-finding (DF) architectures [5, 6, 7, 8, 9, 10]. Their gain, however, is typically lower than that of horn antennas. Achieving high-gain CP operation over a broad frequency range with a horn antenna, without resorting to a dual-feed arrangement, therefore remains challenging. A conventional approach is to perform polarization conversion within the feed network using septum or waveguide polarizers [11, 12, 13, 14, 15, 16]. The usable bandwidth of such waveguide components can nevertheless limit wideband systems.

An alternative is to perform polarization conversion after the antenna aperture using a transmissive polarization converter [17]. For broadband operation, the converter should provide the required differential phase while maintaining low reflection and low transmission loss. Meander-line structures are well suited to this purpose because a multilayer arrangement can convert linear polarization to circular polarization while preserving the underlying radiation pattern [18]. A meander-line unit cell exhibits predominantly inductive and capacitive responses along its two orthogonal principal directions, thereby producing the differential phase required between the transmitted field components [19]. Chu and Lee [20] developed an analytical treatment

of cascaded meander-line boards separated by dielectric spacers for both normal and oblique incidence. For broadband designs, however, a fixed lumped-*L*/*C* representation does not fully capture the distributed frequency response of the printed geometry, particularly toward the upper end of the operating band [21]. A more general approach is therefore to retrieve the frequency-dependent sheet admittance from periodic full-wave unit-cell simulations and use it in a transmission-line model [22]. This strategy has also been used in broadband polarizer optimization with rotated anisotropic sheets [23]. Recent simulation-driven work has similarly used frequency-selective surfaces in compact shared-aperture antenna architectures [24].

In this work, a meander-line linear-to-circular polarization converter is designed for 10–20 GHz. Frequency-dependent equivalent sheet admittances are extracted for a library of meander-line unit cells, and the resulting transmission-line model is used in a hybrid global/local optimization procedure. The contribution is the unified use of full-wave-retrieved broadband sheet admittances, layer-dependent unit cells, independently rotated anisotropic layers, and direct conformal integration of the optimized multilayer polarizer with a cylindrical horn aperture.

The remainder of this paper is organized as follows. Section 2 presents the theoretical model of the multilayer meander-line polarizer, including admittance retrieval and the transfer-matrix formulation. Section 3 validates the semi-analytical model against full-wave simulations and then presents the optimized polarizer and its conformal integration with the horn antenna. Reflection, transmission, axial-ratio, angular, and radiation characteristics are evaluated. Section 4 summarizes the main findings.

2. Theoretical Modeling

The proposed polarizer is modeled as a multilayer transmissive anisotropic structure composed of printed meander-line sheets, dielectric substrates, and spacer regions. The printed sheets provide different electromagnetic responses along two orthogonal transverse directions, while the dielectric and spacer regions control the propagation phase and impedance transformation between successive sheets [18, 19, 20]. Each printed sheet is represented by a shunt admittance tensor and each homogeneous region by a transmission-line matrix. An $e^{j\omega t}$ time convention is assumed throughout, consistent with the inductive and capacitive admittances used below. This formulation is consistent with tensor-based equivalent models for printed metasurfaces and anisotropic sheets [25].

The incident linearly polarized electric field is first decomposed into two orthogonal components referenced to the principal axes of the meander-line unit cell. If the incident electric field makes an angle ϕ_{inc} with the x-axis, the transverse incident field is given by Equation (1) [19, 20].

$$\mathbf{E}_{\text{inc}} = E_0 \cos\phi_{\text{inc}}\,\hat{\mathbf{x}} + E_0 \sin\phi_{\text{inc}}\,\hat{\mathbf{y}}. \tag{1}$$

Here, E_0 is the magnitude of the incident electric field, and $\hat{\mathbf{x}}$ and $\hat{\mathbf{y}}$ are the transverse unit vectors of the unit-cell coordinate system. The corresponding scalar components are given by Equation (2).

$$E_x^{\text{inc}} = E_0 \cos\phi_{\text{inc}}, \qquad E_y^{\text{inc}} = E_0 \sin\phi_{\text{inc}}. \tag{2}$$

For linear-to-circular polarization conversion, the incident polarization is generally chosen as $\phi_{\text{inc}} = 45^\circ$ with respect to the principal axes of the polarizer so that the two incident components have equal magnitudes. The component parallel to the dominant meander-line current path exhibits a predominantly *inductive* response, whereas the orthogonal component exhibits a predominantly *capacitive* response associated with coupling between adjacent conductor sections [19, 21]. The resulting differential phase delay enables polarization conversion. The transmitted field is written as

$$\mathbf{E}_{\text{out}} = E_x^{\text{out}}\hat{\mathbf{x}} + E_y^{\text{out}}\hat{\mathbf{y}}. \tag{3}$$

For the transmitted wave to be circularly polarized, the two orthogonal field components must have equal magnitudes and a quadrature phase difference. In practice, the design seeks the approximate conditions [26]

$$\left|E_x^{\text{out}}\right| \simeq \left|E_y^{\text{out}}\right|, \tag{4}$$

$$\Delta\phi = \angle E_x^{\text{out}} - \angle E_y^{\text{out}} \simeq \pm\frac{\pi}{2}. \tag{5}$$

The sign of the phase difference determines the handedness of the transmitted circularly polarized wave [26].

2.1. Unit Cell Analysis

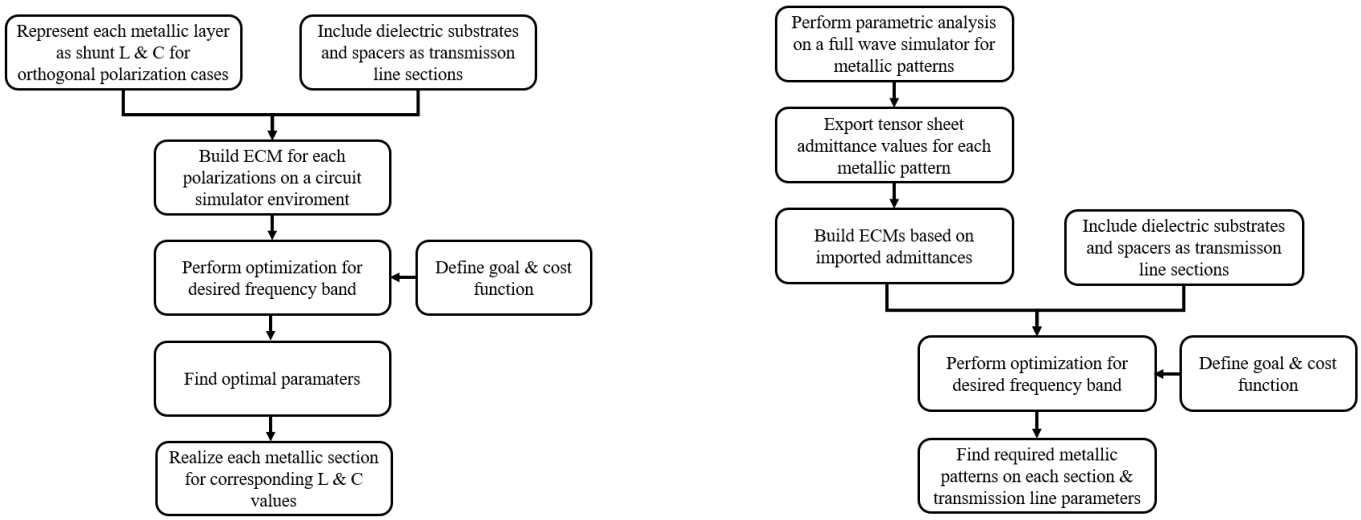
A meander-line unit cell is anisotropic because its response is not invariant under an interchange of its two principal transverse directions. Accordingly, it exhibits distinct equivalent admittances for fields polarized along those directions. When the coordinate axes are aligned with the principal axes of a geometrically symmetric unit cell, the intrinsic cross-coupling terms are negligible and the local sheet response can be described by two principal admittances. This interpretation is commonly used to relate meander-line geometry to polarization-dependent sheet behavior [21].

The first design step is to determine the target admittances for the parallel and perpendicular principal polarizations, as defined in Equation (6), so that the multilayer stack satisfies the required polarization-conversion response.

$$\mathbf{Y}^{\text{tar}}(f) = \left[Y_{\parallel}^{\text{tar}}(f), Y_{\perp}^{\text{tar}}(f)\right] \tag{6}$$

The second step is to realize these target responses through the meander-line geometry. For a narrowband design, the two principal admittances may be approximated by single shunt L and C elements (Subsection 2.2). For broadband operation, however, a fixed lumped-element model does not generally reproduce the distributed frequency response of the printed geometry with sufficient accuracy [21]. The frequency-dependent admittances are therefore retrieved from full-wave unit-cell simulations. The corresponding narrowband and wideband design flows are shown in Figures 1a and 1b, respectively.

In both approaches, the response of the printed metallic pattern must first be characterized. For the normal-incidence retrieval used here, the unit cell is analyzed with periodic boundary conditions and the two orthogonal fundamental Floquet



(a) Design flow for narrowband operation.

(b) Design flow for wideband operation.

Figure 1: Design flows for multilayer meander-line polarizers.

modes, as illustrated in Figure 2. The Floquet reference planes are taken at, or de-embedded to, the printed-sheet plane so that propagation through the surrounding homogeneous layers is represented separately. Under the electric-sheet approximation, in which the tangential electric field is continuous and the discontinuity in tangential magnetic field is represented by a shunt sheet admittance, the tensor admittance of a sheet separating media with modal impedances η_1 and η_2 is obtained from Equation (7) [25].

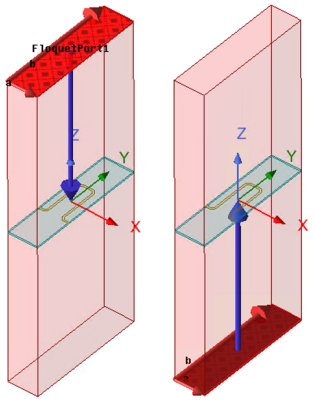


Figure 2: ANSYS HFSS setup for tensor sheet admittance extraction.

$$\mathbf{Y}_s^{\mathrm{loc}} = \left[\frac{\mathbf{I}-\mathbf{S}_{11}}{\eta_1} - \frac{\mathbf{I}+\mathbf{S}_{11}}{\eta_2}\right](\mathbf{I}+\mathbf{S}_{11})^{-1}. \tag{7}$$

In Equation (7), $\mathbf{I}$ is the 2×2 identity matrix and $\mathbf{S}_{11}$ is the reflection matrix in the local principal-axis basis, given by Equation (8). At normal incidence in isotropic media, η_1 and η_2 are the corresponding scalar wave impedances.

$$\mathbf{S}_{11} = \begin{bmatrix} S_{11}^{xx} & S_{11}^{xy} \\ S_{11}^{yx} & S_{11}^{yy} \end{bmatrix} \tag{8}$$

For the ith printed sheet, the local admittance tensor is written as Equation (9).

$$\mathbf{Y}_{s,i}^{\mathrm{loc}} = \begin{bmatrix} Y_{xx,i} & Y_{xy,i} \\ Y_{yx,i} & Y_{yy,i} \end{bmatrix}. \tag{9}$$

In Equation (9), $Y_{xx,i}$ and $Y_{yy,i}$ are the two principal sheet admittances, whereas $Y_{xy,i}$ and $Y_{yx,i}$ represent intrinsic cross-coupling in the local basis. For a reciprocal meander-line pattern with mirror symmetry about its principal axes, these local off-diagonal terms are ideally zero and are negligible in the present retrieval, as confirmed in Subsection 3.1 [27]. This approximation applies only in the local principal-axis basis; rotation of the sheet with respect to the global coordinates generally produces nonzero off-diagonal terms after the tensor transformation.

$$\mathbf{Y}_{s,i}^{\mathrm{loc}} = \begin{bmatrix} Y_{xx,i} & Y_{xy,i} \\ Y_{yx,i} & Y_{yy,i} \end{bmatrix} \approx \begin{bmatrix} Y_{xx,i} & 0 \\ 0 & Y_{yy,i} \end{bmatrix}. \tag{10}$$

With the local cross-coupling neglected, Equations (7) and (10) reduce to the scalar retrieval formulas in Equations (11a) and (11b):

$$Y_{xx,i} = \frac{1-S_{11}^{xx,i}}{\eta_1(1+S_{11}^{xx,i})} - \frac{1}{\eta_2}, \tag{11a}$$

$$Y_{yy,i} = \frac{1-S_{11}^{yy,i}}{\eta_1(1+S_{11}^{yy,i})} - \frac{1}{\eta_2}. \tag{11b}$$

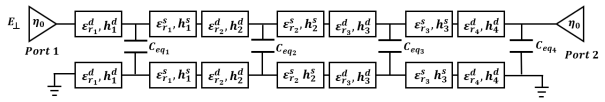
2.2. Design approach for narrowband meander-line polarizers

For narrowband designs, the local principal responses of a meander-line unit cell may be represented by a shunt inductance for the parallel polarization and a shunt capacitance for

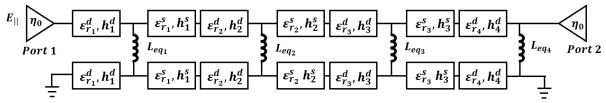
the perpendicular polarization [20, 28]. Equation (10) then reduces to Equation (12).

$$\mathbf{Y}_{s,i}^{\mathrm{loc}} \approx \begin{bmatrix} Y_{\parallel,i} & 0 \\ 0 & Y_{\perp,i} \end{bmatrix} = \begin{bmatrix} \dfrac{1}{j\omega L_{\mathrm{eq},i}} & 0 \\ 0 & j\omega C_{\mathrm{eq},i} \end{bmatrix}. \tag{12}$$

The dielectric substrates and spacers are modeled as transmission-line sections, leading to the equivalent circuit models (ECMs) for the two principal polarizations shown in Figure 3.



(a) ECM for perpendicular polarization case.



(b) ECM for parallel polarization case.

Figure 3: ECM model for a 4-layer narrowband meander-line polarizer.

The relative permittivities of the substrate and spacer associated with each layer are denoted by $\varepsilon_{r,i}^{d}$ and $\varepsilon_{r,i}^{s}$, respectively. For the four-layer example in Figure 3, $i = 1,\ldots,4$ for the substrate/ML sections and $i = 1,\ldots,3$ for the spacers. Their corresponding thicknesses are h_i^d and h_i^s, and η_0 denotes the free-space wave impedance. The equivalent inductance $L_{\mathrm{eq},i}$ and capacitance $C_{\mathrm{eq},i}$ are associated with the parallel and perpendicular principal polarizations, respectively. These values can be realized by optimizing the geometrical parameters of the meander-line unit cells [28].

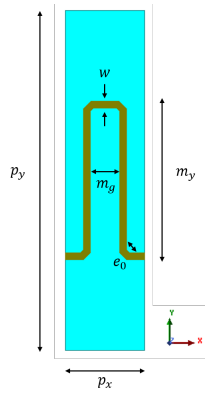


Figure 4: Geometrical parameters of the meander-line unit cell.

The geometrical design variables of a representative meander-line unit cell are collected in Equation (13); the entries may be adapted to the selected unit-cell topology.

$$\mathbf{p} = \begin{bmatrix} p_x & p_y & m_y & m_g & w & e_0 \end{bmatrix}^T. \tag{13}$$

The full-wave-extracted admittance for the parallel polarization is matched to the target inductive response according to Equation (14). Admittance-based unit-cell synthesis of this type is consistent with transmissive metasurface design procedures based on periodic full-wave simulations [22, 23].

$$\left| Y_{\parallel,i}(\mathbf{p},f) - \frac{1}{j2\pi f L_{\mathrm{eq},i}} \right| \le \varepsilon_1. \tag{14}$$

Likewise, the perpendicular admittance is matched to the target capacitive response according to Equation (15).

$$\left| Y_{\perp,i}(\mathbf{p},f) - j2\pi f C_{\mathrm{eq},i} \right| \le \varepsilon_2. \tag{15}$$

In Equations (14) and (15), ε_1 and ε_2 are the unit-cell optimization tolerances. This matching step links the printed geometry to the circuit-level design targets. An application of this approach was previously presented by the authors [29].

2.3. Design approach for wideband meander-line polarizers

For broadband multilayer analysis, the printed meander-line sheet is represented by the frequency-dependent two-dimensional shunt admittance tensor of Equation (9), rather than by fixed scalar L/C elements. A tensor formulation is required once anisotropic sheets are rotated with respect to one another, because the response in the global coordinate system can then contain cross-polarized terms even when the local principal-axis tensor is diagonal [25, 30]. The printed sheet is treated as an electric shunt discontinuity: the transverse electric field is continuous across the sheet, while the tangential magnetic field has the jump associated with the sheet current [25]. With the state convention introduced below, the transfer matrix of the ith meander-line (ML) sheet is

$$\mathbf{T}_{\mathrm{ML},i} = \begin{bmatrix} 1 & 0 & 0 & 0 \\ 0 & 1 & 0 & 0 \\ Y_{xx,i} & Y_{xy,i} & 1 & 0 \\ Y_{yx,i} & Y_{yy,i} & 0 & 1 \end{bmatrix}. \tag{16}$$

For an unrotated layer, the admittance entries in Equation (16) are those of the local tensor. For a rotated layer, they are replaced by the corresponding elements of the global tensor defined in Equation (19). The tensor is obtained from the periodic full-wave retrieval described above. In the transfer-matrix formulation of Equation (16), each transverse electric-field component is paired with the magnetic-field component that carries power in the $+z$ direction. Thus, E_x is paired with H_y, whereas E_y is paired with $-H_x$, and the state vector is defined as

$$\mathbf{f}(z) = \begin{bmatrix} E_x(z) \\ E_y(z) \\ H_y(z) \\ -H_x(z) \end{bmatrix}. \tag{17}$$

With this convention, the printed sheet and each homogeneous region can be cascaded within the same transfer-matrix framework. Because the retrieved admittance retains the frequency dependence of the periodic full-wave unit-cell response, it provides a more appropriate broadband representation than a fixed lumped-element approximation [21, 25]. Once the unit-cell admittance library has been generated, candidate multilayer stacks are evaluated by low-order matrix operations rather than

by repeating a full-wave solution of the complete polarizer for every optimization candidate; full-wave analysis is then used for unit-cell characterization and final validation.

If the principal axes of the ith sheet are rotated by ϕ_i with respect to the global x–y coordinates, the local tensor is transformed using the two-dimensional rotation matrix in Equation (18) [23, 25].

$$\mathbf{R}(\phi_i) = \begin{bmatrix} \cos\phi_i & -\sin\phi_i \\ \sin\phi_i & \cos\phi_i \end{bmatrix}. \tag{18}$$

The corresponding tensor in the global coordinate system is

$$\mathbf{Y}^{\mathrm{g}}_{s,i}(\phi_i) = \mathbf{R}(\phi_i)\mathbf{Y}^{\mathrm{loc}}_{s,i}\mathbf{R}^T(\phi_i). \tag{19}$$

Because $\mathbf{R}$ is orthogonal, $\mathbf{R}^T = \mathbf{R}^{-1}$. Equation (19) shows explicitly that a diagonal local tensor generally becomes non-diagonal after rotation. The rotation angles therefore provide additional degrees of freedom for controlling the amplitude and phase balance of the transmitted components over a wide band [23]. The dielectric substrates and spacer regions are modeled as homogeneous transmission-line sections.

For the ith homogeneous layer of thickness h_i, the propagation phase delay is defined by Equation (20). This representation is standard in transmission-line analyses of cascaded dielectric regions in multilayer meander-line polarizers [18, 20, 31].

$$\psi_i = k_{z,i} h_i. \tag{20}$$

In Equation (20), $k_{z,i}$ is the longitudinal propagation constant inside the ith layer. For normal incidence, this propagation constant is given by:

$$k_{z,i} = k_0\sqrt{\varepsilon_{r,i}}. \tag{21}$$

Here, k_0 is the free-space wavenumber and $\varepsilon_{r,i}$ is the relative permittivity of the ith homogeneous, isotropic, nonmagnetic layer. Under the same normal-incidence assumption, its wave impedance is

$$\eta_i = \frac{\eta_0}{\sqrt{\varepsilon_{r,i}}}. \tag{22}$$

In Equation (22), η_0 is the free-space wave impedance. The transfer matrix of the ith homogeneous dielectric layer (DL) is then

$$\mathbf{T}_{\mathrm{DL},i} = \begin{bmatrix} \cos\psi_i & 0 & j\eta_i\sin\psi_i & 0 \\ 0 & \cos\psi_i & 0 & j\eta_i\sin\psi_i \\ j\eta_i^{-1}\sin\psi_i & 0 & \cos\psi_i & 0 \\ 0 & j\eta_i^{-1}\sin\psi_i & 0 & \cos\psi_i \end{bmatrix}. \tag{23}$$

Equation (23) assumes an isotropic homogeneous layer, so it does not couple the two transverse polarizations; anisotropic coupling is introduced by the printed-sheet tensors. For oblique incidence, the propagation phase is determined by the longitudinal wavenumber component [20, 28]:

$$k_{z,i} = k_0\sqrt{\varepsilon_{r,i}}\cos\theta_i. \tag{24}$$

Here, θ_i is the propagation angle inside the ith layer, measured from the layer normal and obtained from Snell's law. The wave impedance also depends on polarization with respect to the plane of incidence. For TE polarization,

$$\eta_i^{\mathrm{TE}} = \frac{\eta_0}{\sqrt{\varepsilon_{r,i}}\cos\theta_i}. \tag{25}$$

whereas for TM polarization,

$$\eta_i^{\mathrm{TM}} = \frac{\eta_0\cos\theta_i}{\sqrt{\varepsilon_{r,i}}}. \tag{26}$$

Equations (24)–(26) provide the propagation and impedance quantities required for plane-wave angular-response analysis. This is relevant because a multilayer polarizer can be sensitive to incidence angle [20, 28]. In the antenna-integrated configuration, the aperture illumination is not a uniform plane wave; the oblique-incidence model is therefore used as an engineering indicator of E- and H-plane angular stability rather than as an exact representation of the complete aperture field.

The response of the complete multilayer polarizer is obtained by cascading the printed-sheet and homogeneous-layer matrices in their physical order. For an N-sheet polarizer, the total transfer matrix is [20, 25]

$$\mathbf{T}_{\mathrm{tot}} = \mathbf{T}_{\mathrm{ML},1}\mathbf{T}_{\mathrm{DL},1}\mathbf{T}_{\mathrm{ML},2}\mathbf{T}_{\mathrm{DL},2}\cdots\mathbf{T}_{\mathrm{DL},N-1}\mathbf{T}_{\mathrm{ML},N}. \tag{27}$$

Here, $\mathbf{T}_{\mathrm{ML},i}$ is the transfer matrix of the ith meander-line sheet and $\mathbf{T}_{\mathrm{DL},i}$ denotes the ordered transfer matrix of the homogeneous region between consecutive sheets. If that region contains more than one material section, such as a substrate followed by an air spacer, $\mathbf{T}_{\mathrm{DL},i}$ is the product of the corresponding homogeneous-section matrices. Any homogeneous section before the first sheet or after the last sheet is included in the same manner. The total matrix is partitioned into four 2×2 blocks:

$$\mathbf{T}_{\mathrm{tot}} = \begin{bmatrix} \mathbf{A} & \mathbf{B} \\ \mathbf{C} & \mathbf{D} \end{bmatrix}. \tag{28}$$

The block matrices $\mathbf{A}$, $\mathbf{B}$, $\mathbf{C}$, and $\mathbf{D}$ contain the complete coupled transfer response of the multilayer stack. The first two blocks are

$$\mathbf{A} = \begin{bmatrix} A_{xx} & A_{xy} \\ A_{yx} & A_{yy} \end{bmatrix}, \qquad \mathbf{B} = \begin{bmatrix} B_{xx} & B_{xy} \\ B_{yx} & B_{yy} \end{bmatrix}. \tag{29}$$

and the remaining two are

$$\mathbf{C} = \begin{bmatrix} C_{xx} & C_{xy} \\ C_{yx} & C_{yy} \end{bmatrix}, \qquad \mathbf{D} = \begin{bmatrix} D_{xx} & D_{xy} \\ D_{yx} & D_{yy} \end{bmatrix}. \tag{30}$$

The off-diagonal elements in Equations (29) and (30) describe coupling between the two transverse polarizations after cascading the rotated anisotropic sheets. For normal incidence with the same isotropic reference medium of impedance η_0 on both sides of the stack, the forward-transmission and input-reflection matrices follow directly from the ABCD blocks:

$$\mathbf{S}_{21} = 2\left(\mathbf{A} + \frac{\mathbf{B}}{\eta_0} + \eta_0\mathbf{C} + \mathbf{D}\right)^{-1}, \tag{31}$$

$$\mathbf{S}_{11} = \left(\mathbf{A} + \frac{\mathbf{B}}{\eta_0} - \eta_0\mathbf{C} - \mathbf{D}\right)\left(\mathbf{A} + \frac{\mathbf{B}}{\eta_0} + \eta_0\mathbf{C} + \mathbf{D}\right)^{-1}. \quad (32)$$

These matrix relations are the vector extension of the conventional two-port ABCD-to-*S* conversion and are consistent with the state vector in Equation (17) [25]. The resulting scattering representation can be written as

$$\begin{bmatrix}\mathbf{b}_1\\ \mathbf{b}_2\end{bmatrix} = \begin{bmatrix}\mathbf{S}_{11} & \mathbf{S}_{12}\\ \mathbf{S}_{21} & \mathbf{S}_{22}\end{bmatrix}\begin{bmatrix}\mathbf{a}_1\\ \mathbf{a}_2\end{bmatrix}. \quad (33)$$

Here, $\mathbf{a}_1$ and $\mathbf{a}_2$ are the incident-wave vectors at ports 1 and 2, and $\mathbf{b}_1$ and $\mathbf{b}_2$ are the corresponding outgoing-wave vectors. The forward-transmission matrix is

$$\mathbf{S}_{21} = \begin{bmatrix}S_{21}^{xx} & S_{21}^{xy}\\ S_{21}^{yx} & S_{21}^{yy}\end{bmatrix}. \quad (34)$$

For excitation from port 1 only ($\mathbf{a}_2 = 0$), the transmitted electric-field vector is

$$\begin{bmatrix}E_x^{\text{out}}\\ E_y^{\text{out}}\end{bmatrix} = \mathbf{S}_{21}\begin{bmatrix}E_x^{\text{inc}}\\ E_y^{\text{inc}}\end{bmatrix}. \quad (35)$$

The two transmitted components are therefore

$$E_x^{\text{out}} = S_{21}^{xx}E_x^{\text{inc}} + S_{21}^{xy}E_y^{\text{inc}}, \quad (36)$$

$$E_y^{\text{out}} = S_{21}^{yx}E_x^{\text{inc}} + S_{21}^{yy}E_y^{\text{inc}}. \quad (37)$$

Thus, both co-polarized and cross-polarized transmission terms contribute to the output when anisotropic layers are rotated. The phase difference between the two transmitted components is

$$\Delta\phi = \angle E_x^{\text{out}} - \angle E_y^{\text{out}}. \quad (38)$$

The corresponding linear axial ratio is [26]

$$\text{AR} = \sqrt{\frac{|E_x^{\text{out}}|^2 + |E_y^{\text{out}}|^2 + \sqrt{\alpha}}{|E_x^{\text{out}}|^2 + |E_y^{\text{out}}|^2 - \sqrt{\alpha}}}. \quad (39)$$

where

$$\alpha = |E_x^{\text{out}}|^4 + |E_y^{\text{out}}|^4 + 2|E_x^{\text{out}}|^2|E_y^{\text{out}}|^2\cos(2\Delta\phi). \quad (40)$$

For identical isotropic media on the input and output sides, the field-amplitude transmission magnitude for the specified incident polarization is

$$|T| = \frac{\sqrt{|E_x^{\text{out}}|^2 + |E_y^{\text{out}}|^2}}{\sqrt{|E_x^{\text{inc}}|^2 + |E_y^{\text{inc}}|^2}}. \quad (41)$$

Under the same identical-medium assumption, the transmitted power fraction is $|T|^2$ and the insertion loss is $-20\log_{10}|T|$ dB. For unequal media, the corresponding wave-impedance normalization must be included.

The design is optimized over sampled frequencies f_i, $i = 1, 2, \ldots, N_f$. The objective penalizes violations of the axial-ratio and co-polarized transmission targets across the prescribed band. A threshold-based form is used [18, 23]:

$$\begin{aligned}\mathscr{C} =& W_{\text{AR}}\sum_{i=1}^{N_f}\left[\max\left(0, \text{AR}_{\text{dB}}(f_i) - \text{AR}_{\text{th}}\right)\right]^2\\ &+ W_x\sum_{i=1}^{N_f}\left[\max\left(0, T_{\text{th}} - |S_{21}^{xx}(f_i)|\right)\right]^2\\ &+ W_y\sum_{i=1}^{N_f}\left[\max\left(0, T_{\text{th}} - |S_{21}^{yy}(f_i)|\right)\right]^2.\end{aligned} \quad (42)$$

In Equation (42), W_{AR}, W_x, and W_y are weighting factors, AR_{th} is the axial-ratio threshold, and T_{th} is the minimum acceptable magnitude of each co-polarized transmission term. The max operator ensures that only frequency samples that violate a specified target contribute to the cost.

In summary, the theoretical framework has two stages. The frequency-dependent unit-cell response is first obtained from periodic full-wave simulations and represented by a local admittance tensor. The complete multilayer response is then evaluated by rotating the required sheet tensors into the global coordinate system and cascading them with the homogeneous transmission-line sections.

3. Numerical Analysis

The numerical study is organized in two steps. First, the wideband design procedure of Figure 1b is validated using a multilayer test polarizer by comparing the MATLAB semi-analytical model with ANSYS HFSS. The validated framework is then used to design a five-layer polarizer for 10–20 GHz, after which the optimized structure is conformed to and integrated with the cylindrical aperture of a horn antenna.

3.1. Full-wave validation

A five-layer test polarizer was designed over 8–18 GHz using a single unit-cell geometry, with targets of AR < 3 dB and reflection below -10 dB for both principal polarizations. A genetic algorithm (GA) was first used for the global search, followed by local refinement with MATLAB's *fmincon* solver. The resulting parameters are listed in Table 1.

Table 1: Test Polarizer Specifications & Geometric Parameters

General Specifications	
Frequency Range	8–18 GHz
Stack No / Spacer ε_r	5 / 1.0 (Air)
Substrate	Rogers 5880 ($\varepsilon_r = 2.2$, Thk=0.1 mm)
Unit Cell Geometry (mm)	
p_y/p_x	7.5 / 1.75
m_y / e_0 / w_g / w	3.5 / 0.1 / 0.5 / 0.15
Rotation Angle	45°
Inter-Layer Spacer Thicknesses (mm)	
Spacer 1 & 4	3.61
Spacer 2 & 3	5.04

The corresponding ANSYS HFSS model is shown in Figure 5, and Figure 6 compares the full-wave results with the MATLAB model.

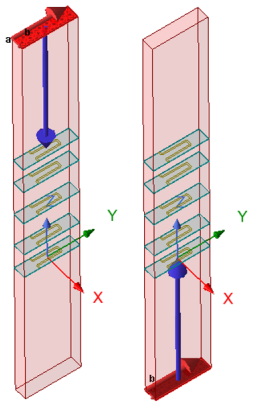
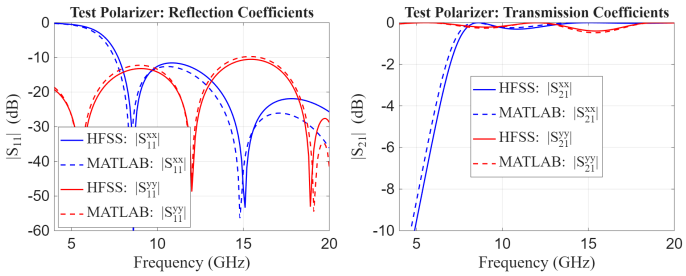
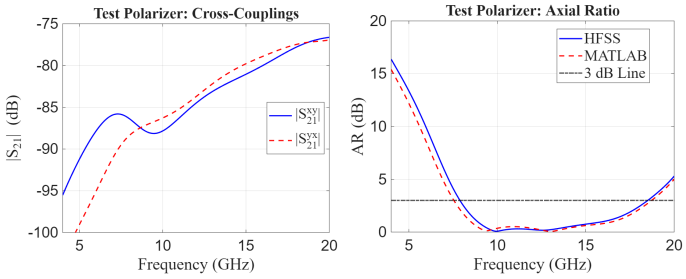


Figure 5: ANSYS HFSS setup for polarizer.



(a) Reflection coefficient comparison. **(b)** Transmission coefficient comparison.



(c) Cross-coupling values. **(d)** AR results.

Figure 6: Comparison with full-wave results.

As shown in Figure 6, the off-diagonal transmission terms of the validation stack remain below approximately -77 dB over the plotted range. This result supports neglecting intrinsic cross-coupling in the local principal-axis unit-cell retrieval for the geometry considered here. It does not remove the coupling generated by intentional layer rotation, which is retained through the tensor transformation in Equation (19). The calculated co-polarized S-parameters and the resulting axial ratio are in good agreement with the full-wave results.

3.2. Polarizer design: integrated results

A five-layer polarizer with the symmetric cell 1–2–3–2–1 sequence and independently rotated layers was then designed for horn-antenna integration. Its specifications and optimized geometrical parameters are listed in Table 2.

Table 2: Specifications & Geometric Parameters of the Designed Polarizer

General Specifications	
Frequency Band	10–20 GHz
Stack Number / Spacer ε_r	5 / 1.0 (Air)
Substrate	Kapton ($\varepsilon_r = 3.4$, Thk=0.1 mm)
Inter-Layer Spacer Thicknesses (mm)	
Spacer 1 & 4	3.30
Spacer 2 & 3	4.87
Unit Cell Geometry (mm & °)	
Fixed Parameters	$p_y/p_x = 7.5/1.75$, $e = 0.1$, $w_g = 0.7$
Cell 1 (m_y / w / *Rot.*)	3.0 / 0.200 / 46.00°
Cell 2 (m_y / w / *Rot.*)	3.2 / 0.125 / 38.77°
Cell 3 (m_y / w / *Rot.*)	3.0 / 0.275 / 50.07°

The optimized axial-ratio, transmission, and reflection responses are shown in Figure 7.

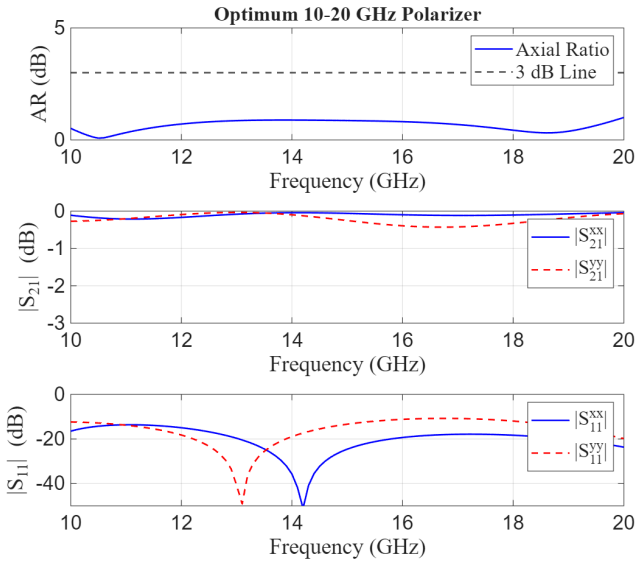
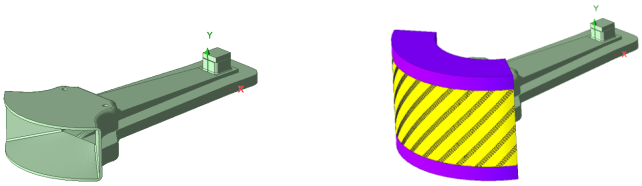


Figure 7: Optimized response of the designed polarizer.

The optimized planar polarizer was then mapped onto the cylindrical aperture of the horn using radius-dependent scaling of the meander-line gaps [32, 33]. The first layer serves as the reference; subsequent layers are scaled in proportion to their cylindrical radii along the x-direction, which is the bending direction, while the y-dimensions are kept unchanged under the line-source approximation used for the integration. A 2-mm separation is retained between the antenna aperture and the first polarizer layer for impedance matching. LS-18 absorber is placed along the E-plane edges to reduce edge diffraction. Front views of the antenna with and without the polarizer are shown in Figure 8.

A detailed view of the integrated multilayer polarizer is provided in Figure 9.

Figure 10 compares the input reflection and realized gain of the integrated configuration with those of the standalone antenna. The polarizer preserves the antenna matching, with $|S_{11}|_{\mathrm{dB}} < -10$ dB over the operating band, and introduces a maximum insertion loss of 0.55 dB.



(a) Antenna only. **(b)** Antenna with polarizer.

Figure 8: Horn antenna before and after polarizer integration.

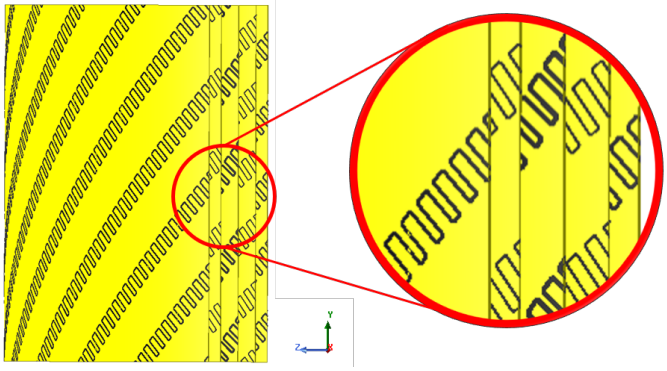
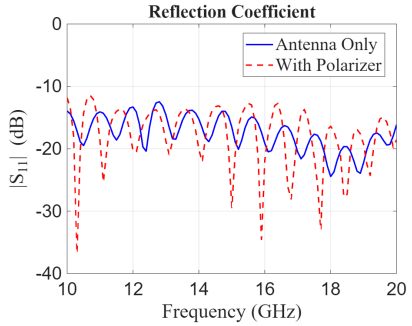
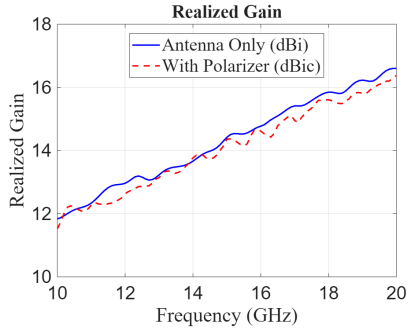


Figure 9: Detailed view of polarizer.



(a) $|S_{11}|$ comparison.



(b) Realized gain comparison.

Figure 10: Input-reflection and realized-gain comparison before and after polarizer integration.

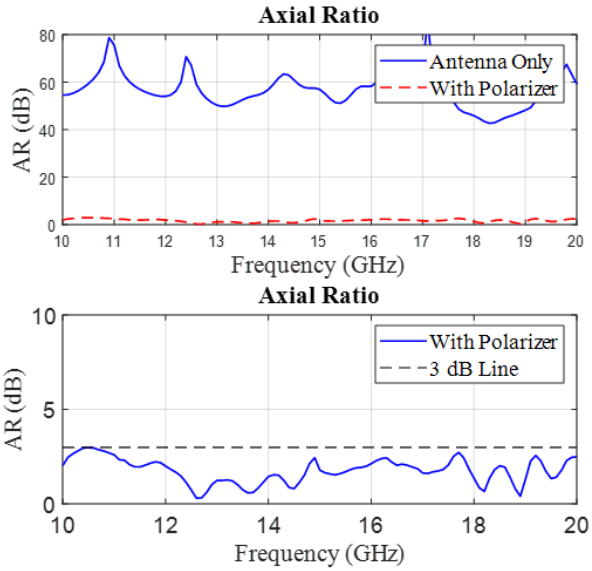


Figure 11: Boresight axial-ratio comparison before and after polarizer integration.

The boresight axial ratios of the integrated system and the standalone antenna are compared in Figure 11.

At representative frequencies, the E- and H-plane radiation patterns are compared in Figure 12. The comparison shows that the added metallic layers do not materially distort the principal radiation patterns.

The angular response of the integrated system is examined in Figure 13. Because the polarizer is cylindrically curved along the x-direction (H-plane), the local incidence angle on the polarizer is reduced away from boresight in that plane. This geometry therefore provides greater H-plane angular stability than the corresponding planar orientation in the E-plane.

The nominal half-power beamwidths (HPBWs) are 30° (±15°) in the E-plane and 40° (±20°) in the H-plane. Over these angular ranges, the polarizer maintains the intended polarization conversion across the antenna main beam. Figure 14 presents the co- and cross-polarized patterns at representative frequencies. After linear-to-circular conversion, the cross-polarization discrimination (XPD) remains between 16 and 20 dB.

Table 3 places the proposed design alongside representative transmissive LCPCs from the literature. The 3-dB axial-ratio and −10-dB reflection bands are listed separately because satisfactory polarization conversion does not always coincide with good impedance matching. Values not explicitly reported are identified as being read from plots, recalculated from published dimensions, or conservatively inferred from transmission data; entries that cannot be established reliably are marked as NR. Although several planar designs perform well in individual metrics, conformal implementations are better suited to cylindrical and omnidirectional apertures, making them particularly attractive for close-range applications despite their generally narrower reported bandwidths. The proposed cylindrical-aperture polarizer achieves a 66.6% 3-dB axial-ratio bandwidth and a maximum insertion loss of 0.55 dB while maintaining stable performance under oblique incidence.

Table 3: Comparison of representative transmissive LCPC designs.

Work	Topology	Structure type	3-dB AR band (GHz)	AR FBW (%)	−10-dB reflection band (GHz)	Max. IL (dB)	Total t (mm)	$t/\lambda_0(f_H)$	Angular stability with AR < 3 dB
[34]	ML	Planar	$\leq$ 16.0–$\geq$ 23.0*§	$>$ 35.9*§	$\sim$ 16.3–$\sim$ 20.7*‡§	$\sim$ 0.8*§	3.95†	$\geq$ 0.303†	$\pm60°$* ($\phi=0°$) $\pm60°$* ($\phi=90°$)
[35]	Hybrid ML–loop	Planar	18.0–29.0*	46.8*	NB	$\sim$ 3.0*	0.254	0.0246†	30° ($\phi=0°,90°$)
[36]	MEFSS	Planar	8.00–12.00*	40.0*	$\sim$ 8.2–$\sim$ 9.0*‡§	$<$ 2.7*	5.40	0.216†	$\pm45°$* (xz) $\pm45°$* (yz)
[37]	Modified JC	Planar	18.0–21.9	20.0	18.0–21.9‡	$\leq$ 0.40	3.15†	0.230†	$\pm45°$ (ZX/ZY) worst-plane FBW: 1.2%
[38]	Composite cross FSS	Planar	5.75–11.20*	64.3*	$\sim$ 6.2–$\sim$ 8.0‡§	$<$ 1.5	8.00†	0.299†	20°* ($\phi=0°$)
[39]	Multilayer MS	Planar	24.84–30.24*	19.6*	24.0–34.0	$<$ 0.5*	12.0	1.210†	0°–50°* ($\phi=0°$) 0°–50° (sim., $\phi=0°,45°,90°$)
[40]	Grid–patch FSS	Planar	11.36–17.83	44.6	$\leq$ 11.0–$\sim$ 16.2*§	$<$ 1.5*	6.00	0.357†	$\pm50°$* (xz) $\pm50°$* (yz)
[41]	Bi-layer MS	Planar	7.63–11.13	37.3	$\sim$ 10.0–$\sim$ 11.1§	2.19	2.40	0.0891†	75° (TE, xz; simulated)
[42]	Double-U slot FSS	Planar	$\sim$ 7.3–$\sim$ 10.6*§	36.6*	$\sim$ 8.5–$\sim$ 10.0*§	$<$ 3.0*	1.00	0.0354†	$\pm60°$* (xz) $\pm60°$* (yz)
[43]	Cross–strip MS	Planar	15.3–33.1*	74.0*	NB	$<$ 3.0* (70% common BW)	1.575	0.174†	55°* (xz) 55°* (yz)
[44]	Crossed-dipole MS	Planar	11.66–30.12*	88.4*	NR	2.4*	0.508	0.0510†	$\pm40°$ (sim.; plane NR)
[45]	Meandered-strip MS	Planar	6.00–12.85* (TE) 5.50–12.90* (TM)	72.6* (TE) 80.4* (TM)	NR	2.6* (TE) 2.2* (TM)	0.127	0.00547†	60°* (TE) 60°* (TM)
[32]	Wrapped ML	Conformal	$\sim$ 2.37–$\sim$ 2.70*§	$\sim$ 13.0*§	$\sim$ 2.20–$\sim$ 2.55§‖	NR	NR#	NR	$\sim\pm45°$*§ (plane NR)
[33]	Wrapped ML	Conformal	7.00–8.70§♭	$\geq$ 21.7§♭	7.00–8.70§♭	NR	19.27†	0.559†	$\pm20°$ (RX, integrated) TX: AR > 3 dB at boresight
This work	Wrapped ML	Conformal	10.00–20.00	66.6	10.00–20.00	0.55	16.84¶	1.123¶	$\pm20°/\pm25°$ (E/H)

*Measured result. †Calculated from the physical dimensions or electrical thickness given in the cited study. The free-space wavelength λ_0 is evaluated at the upper limit f_H of the reported 3-dB axial-ratio band. ‡Conservative estimate of the −10-dB reflection band. For a passive structure, $T_{tot} > -0.458$ dB guarantees that the total reflected power is below −10 dB. These values are therefore inferred from the reported transmission response rather than taken from a directly reported reflection bandwidth. §Approximate value obtained by reading the corresponding curve in the cited study. ‖This band is taken from the simulated S_{11} response of the combined vibrator–polarizer configuration. The study does not explicitly confirm that the plotted response corresponds to the measured three-layer prototype. #Although a substrate thickness of 0.25 mm is specified for each sheet, the spacing between successive sheets is not given. The total profile can therefore not be determined reliably. ♭The AR and reflection bands are obtained from the infinite planar three-layer model before the structure is wrapped around the cylindrical surface. The angular result, in contrast, refers to the integrated conformal antenna operating in the RX band. ¶For the proposed design, the total thickness is calculated as $5(0.1)+2(3.30)+2(4.87)=16.84$ mm. The 2-mm separation between the antenna and the polarizer is not included. NB indicates that the available results do not contain a common frequency interval satisfying the −10-dB reflection criterion. NR indicates that the relevant value was not reported and could not be reliably extracted using a consistent definition. ML: meander line; JC: Jerusalem cross; MS: metasurface; MEFSS: miniaturized-element frequency-selective surface.

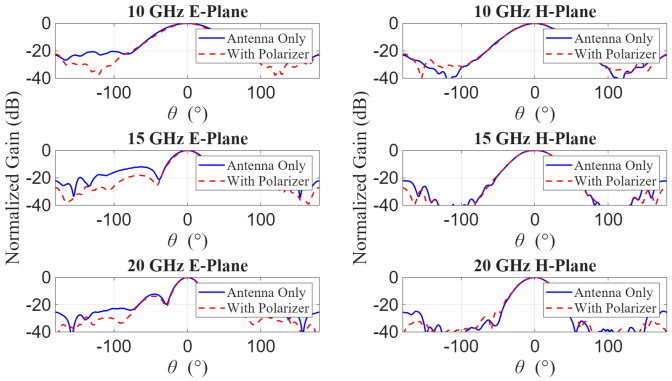


Figure 12: Radiation pattern comparison.

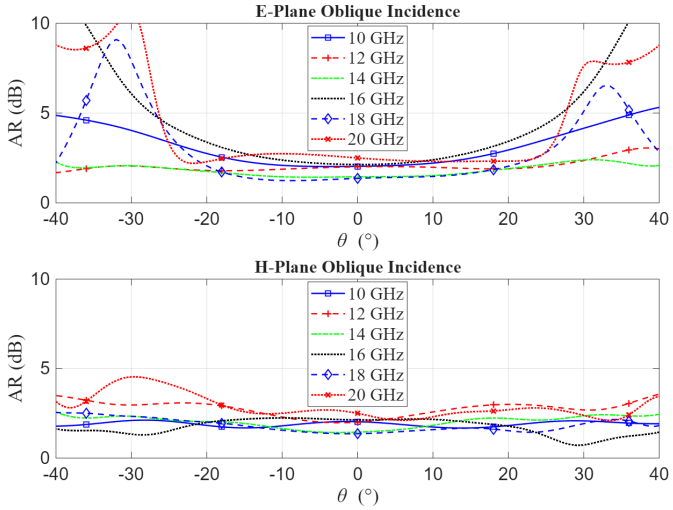


Figure 13: Oblique incidence performance.

4. Conclusion

A broadband conformal meander-line polarizer integrated with a cylindrical horn aperture has been presented. The design procedure combines frequency-dependent full-wave unit-cell admittance retrieval, tensor-based transmission-matrix modeling, and hybrid global/local optimization. Its contribution lies in bringing these elements together in a single broadband workflow that supports layer-dependent unit cells, independently rotated anisotropic sheets, and direct conformal integration with a cylin-

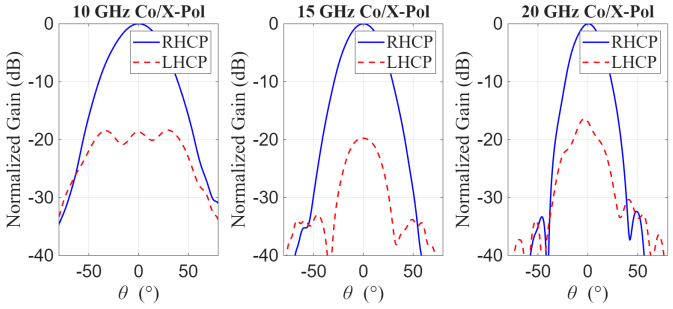


Figure 14: Co- and cross-polarized radiation patterns.

drical antenna aperture. The semi-analytical multilayer model was validated against full-wave simulations before antenna-level integration. The final five-layer conformal configuration achieves a 66.6% 3-dB axial-ratio bandwidth over 10–20 GHz with a maximum insertion loss of 0.55 dB, while preserving the principal radiation patterns and maintaining polarization conversion over the antenna main beam. The present work focuses on development and numerical validation of the design framework; experimental characterization of a fabricated conformal prototype is a natural next step. The results establish the proposed approach as an efficient framework for broadband linear-to-circular polarization conversion on cylindrical antenna apertures.

Acknowledgment

The authors thank ASELSAN Inc. for its support of this work.

References

[1] D. Roddy, *Satellite Communications*, 4th ed. New York, NY, USA: McGraw-Hill, 2006.

[2] A. M. Morey, A. R. Vaidya, and S. S. Kakatkar, "Design and development of spiral antenna for electronic warfare systems," in *Proc. 4th Int. Conf. Range Technol. (ICORT)*, Chandipur, Balasore, India, 2025, pp. 1–5, doi: 10.1109/ICORT64008.2025.11115803.

[3] M. A. Shukoor, S. Dey, and S. Dey, "Broadband and wide angular stable inductive grid-based linear-to-circular transmission-type polarizer for satellite communication applications," in *Proc. IEEE Int. Symp. Antennas Propag. USNC-URSI Radio Sci. Meeting (APS/URSI)*, Singapore, 2021, pp. 569–570, doi: 10.1109/APS/URSI47566.2021.9703765.

[4] F. Neri, *Introduction to Electronic Defense Systems*, 3rd ed. Norwood, MA, USA: Artech House, 2018.

[5] T. E. Morgan, "Spiral antennas for ESM," *IEE Proceedings F (Communications, Radar and Signal Processing)*, vol. 132, no. 4, pp. 245–251, 1985, doi: 10.1049/ip-f-1.1985.0057.

[6] M. Elmansouri, L. Boskovic, and D. Filipovic, "3:1 Bandwidth Sinuous Antenna for Direction Finding Applications," in *2022 16th European Conference on Antennas and Propagation (EuCAP)*, 2022, pp. 1–5, doi: 10.23919/EuCAP53622.2022.9769664.

[7] H. S. Zhang, K. Xiao, L. Qiu, and S. L. Chai, "Four-arm sinuous antenna for direction finding system," in *2014 IEEE International Wireless Symposium (IWS 2014)*, 2014, pp. 1–4, doi: 10.1109/IEEE-IWS.2014.6864258.

[8] A. Mousavikhah, V. Nayyeri, and M. Khanjarian, "An Ultrawideband Spiral Antenna With a Stable Phase Center," *IEEE Access*, vol. 12, pp. 106313–106320, 2024, doi: 10.1109/ACCESS.2024.3437242.

[9] G. L. A. Maturi, S. Koduru, M. Narisetty, S. D. R. V, D. G. Kurup, and P. Vijayvergiya, "Design and Simulation of a Compact Unidirectional Spiral Antenna with Improved Axial Ratio For Electronic Support Measures Application," in *2024 5th IEEE Global Conference for Advancement in Technology (GCAT)*, 2024, pp. 1–6, doi: 10.1109/GCAT62922.2024.10923867.

[10] D. Adamy, *EW 101: A First Course in Electronic Warfare*. Boston, MA: Artech House, 2001.

[11] V. Akan, "S-Bant adımlı septum kutuplaştırıcı tasarımı ve analizi" [S-band stepped septum polarizer design and analysis] (in Turkish), *Iğdır Üniversitesi Fen Bilimleri Enstitüsü Dergisi*, vol. 11, no. 1, pp. 145–156, 2021, doi: 10.21597/jist.775132.

[12] F. Dubrovka, S. Piltyay, O. Sushko, R. Dubrovka, M. Lytvyn, and S. Lytvyn, "Compact X-band stepped-thickness septum polarizer," in *2020 IEEE Ukrainian Microwave Week (UkrMW)*, 2020, pp. 135–138, doi: 10.1109/UkrMW49653.2020.9252583.

[13] Y. L. Chen, T. Chiueh, and H. F. Teng, "A 77-118 GHz resonance-free septum polarizer," *The Astrophysical Journal Supplement Series*, vol. 211, no. 1, Art. no. 11, 2014, doi: 10.1088/0067-0049/211/1/11.

[14] G. Jazani and A. Pirhadi, "Design of dual-polarised (RHCP/LHCP) quad-ridged horn antenna with wideband septum polariser waveguide feed," *IET Microwaves, Antennas & Propagation*, vol. 12, no. 9, pp. 1541–1545, 2018, doi: 10.1049/iet-map.2017.0611.

[15] S. I. Piltyay, A. V. Bulashenko, and I. V. Demchenko, "Waveguide iris polarizers for Ku-band satellite antenna feeds," *Journal of Nano- and Electronic Physics*, vol. 12, no. 5, Art. no. 05024, 2020, doi: 10.21272/jnep.12(5).05024.

[16] S. I. Piltyay, A. V. Bulashenko, and Y. I. Kalinichenko, "Analysis of waveguide polarizers using equivalent network and finite elements methods," *Journal of Electromagnetic Waves and Applications*, vol. 36, no. 12, pp. 1633–1655, 2022, doi: 10.1080/09205071.2022.2037471.

[17] A. M. Hakimi, A. Keivaan, H. Oraizi, and A. Amini, "Wide-scanning circularly polarized reflector-based modulated metasurface antenna enabled by a broadband polarizer," *IEEE Trans. Antennas Propag.*, vol. 70, no. 1, pp. 84–96, Jan. 2022, doi: 10.1109/TAP.2021.3096315.

[18] W. Abdouni-Abdallah, M. S. Khan, and A. Konstantinidis, "Design of a wideband multilayer meander-line polarizer (6–18 GHz) using a semi-analytical method," in *Proc. 48th*

European Microwave Conference (EuMC), Madrid, Spain, 2018, pp. 137–140, doi: 10.23919/EuMC.2018.8541675.

[19] L. Young, L. Robinson, and C. Hacking, "Meander-line polarizer," *IEEE Transactions on Antennas and Propagation*, vol. 21, no. 3, pp. 376–378, May 1973, doi: 10.1109/TAP.1973.1140503.

[20] R.-S. Chu and K.-M. Lee, "Analytical method of a multilayered meander-line polarizer plate with normal and oblique plane-wave incidence," *IEEE Transactions on Antennas and Propagation*, vol. 35, no. 6, pp. 652–661, Jun. 1987, doi: 10.1109/TAP.1987.1144158.

[21] R. Vincenti Gatti and R. Rossi, "A novel meander-line polarizer modeling procedure and broadband equivalent circuit," *IEEE Transactions on Antennas and Propagation*, vol. 65, no. 11, pp. 6179–6184, Nov. 2017, doi: 10.1109/TAP.2017.2754471.

[22] X. You, C. Fumeaux, and W. Withayachumnankul, "Tutorial on broadband transmissive metasurfaces for wavefront and polarization control of terahertz waves," *Journal of Applied Physics*, vol. 131, no. 6, Art. no. 061101, Feb. 2022, doi: 10.1063/5.0077652.

[23] C. Pfeiffer and B. Tomasic, "Linear-to-circular polarizers for multi-octave bandwidths and wide scan angles at mm-wave frequencies using rotated anisotropic layers," *Progress In Electromagnetics Research C*, vol. 79, pp. 49–64, 2017, doi: 10.2528/PIERC17081101.

[24] M. Räsänen, J. Ala-Laurinaho, A. Di Giovanni, J. M. Fernández Gonzalez, A. T. Muriel-Barrado, and V. Viikari, "Profile-reduced S/X-band shared-aperture antenna array with frequency-selective surfaces," *Reviews of Electromagnetics*, vol. 4, 2025, doi: 10.53792/RoE/2025/25015.

[25] R. Shavit and Y. Tzabari, "Tensor surface impedance modelling of metasurfaces with printed elements," *IET Microwaves, Antennas & Propagation*, vol. 17, no. 10, pp. 807–817, 2023, doi: 10.1049/mia2.12397.

[26] C. A. Balanis, *Antenna Theory: Analysis and Design*, 4th ed. Hoboken, NJ, USA: Wiley, 2016.

[27] M. Borgese and F. Costa, "A simple equivalent circuit approach for anisotropic frequency-selective surfaces and metasurfaces," *IEEE Transactions on Antennas and Propagation*, vol. 68, no. 10, pp. 7088–7098, Oct. 2020, doi: 10.1109/TAP.2020.3008658.

[28] M. Letizia, B. Fuchs, C. Zorraquino, J.-F. Zurcher, and J. R. Mosig, "Oblique-incidence design of meander-line polarizers for dielectric lens antennas," *Progress In Electromagnetics Research B*, vol. 45, pp. 309–335, 2012, doi: 10.2528/PIERB12080807.

[29] A. E. Gürsoy, M. Kuloğlu, and K. Karaçuha, "Broadband conformal meander-line polarizer: Equivalent circuit modeling and cylindrical aperture integration," in *Proc. 2026 20th European Conference on Antennas and Propagation (EuCAP)*, Dublin, Ireland, 2026, pp. 1–5, doi: 10.23919/EuCAP68105.2026.11612183.

[30] C. Pfeiffer and A. Grbic, "Bianisotropic metasurfaces for optimal polarization control: Analysis and synthesis," *Physical Review Applied*, vol. 2, no. 4, Art. no. 044011, Oct. 2014, doi: 10.1103/PhysRevApplied.2.044011.

[31] N. Marcuvitz, Ed., *Waveguide Handbook*, Radiation Laboratory Series, vol. 10. New York, NY, USA: McGraw-Hill, 1951.

[32] A. V. Stankovsky, S. V. Polenga, A. D. Nemshon, Y. A. Litinskaya, E. R. Gafarov, and Y. P. Salomatov, "Meander-line polarizer for omnidirectional antenna," in *2016 International Siberian Conference on Control and Communications (SIBCON)*, Moscow, Russia, 2016, pp. 1–4, doi: 10.1109/SIBCON.2016.7491857.

[33] S. Olvhammar, "A new circularly polarized biconical horn for spacecraft TT&C," M.S. thesis, Dept. Electrical Engineering, Chalmers University of Technology, Gothenburg, Sweden, 2018. [Online]. Available: https://publications.lib.chalmers.se/records/fulltext/255354/255354.pdf

[34] M.-A. Joyal and J.-J. Laurin, "Analysis and design of thin circular polarizers based on meander lines," *IEEE Transactions on Antennas and Propagation*, vol. 60, no. 6, pp. 3007–3011, Jun. 2012, doi: 10.1109/TAP.2012.2194659.

[35] P. Fei, Z. Shen, X. Wen, and F. Nian, "A single-layer circular polarizer based on hybrid meander line and loop configuration," *IEEE Transactions on Antennas and Propagation*, vol. 63, no. 10, pp. 4609–4614, Oct. 2015, doi: 10.1109/TAP.2015.2462128.

[36] S. M. A. Momeni Hasan Abadi and N. Behdad, "Wideband linear-to-circular polarization converters based on miniaturized-element frequency selective surfaces," *IEEE Transactions on Antennas and Propagation*, vol. 64, no. 2, pp. 525–534, Feb. 2016, doi: 10.1109/TAP.2015.2504999.

[37] M. Hosseini and S. V. Hum, "A circuit-driven design methodology for a circular polarizer based on modified Jerusalem cross grids," *IEEE Transactions on Antennas and Propagation*, vol. 65, no. 10, pp. 5322–5331, Oct. 2017, doi: 10.1109/TAP.2017.2740972.

[38] W. Zhang, J.-Y. Li, and J. Xie, "A broadband circular polarizer based on cross-shaped composite frequency selective surfaces," *IEEE Transactions on Antennas and Propagation*, vol. 65, no. 10, pp. 5623–5627, Oct. 2017, doi: 10.1109/TAP.2017.2735459.

[39] D. Blanco and R. Sauleau, "Broadband and broad-angle multilayer polarizer based on hybrid optimization algorithm for low-cost Ka-band applications," *IEEE Transactions on Antennas and Propagation*, vol. 66, no. 4, pp. 1874–1881, Apr. 2018, doi: 10.1109/TAP.2018.2804618.

[40] H.-M. Hu, D.-F. Zhou, X. Lei, and J.-M. Wu, "A thin and broadband linear-to-circular polarizer based on grid-patch structure for Ku-band," *International Journal of Antennas and Propagation*, vol. 2018, Art. no. 5695987, 2018, doi: 10.1155/2018/5695987.

[41] B. Lin, J. Guo, Y. Wang, Z. Wang, B. Huang, and X. Liu, "A wide-angle and wide-band circular polarizer using a bi-layer metasurface," *Progress In Electromagnetics Research*, vol. 161, pp. 125–133, 2018, doi: 10.2528/PIER18010922.

[42] H. Hu, D. Zhou, G. Chen, T. Li, and J. Gao, "Design of modified single-layer double U-type linear to circular polarization convertor," *International Journal of Antennas and Propagation*, vol. 2019, Art. no. 1604695, 2019, doi: 10.1155/2019/1604695.

[43] H. B. Wang, Y. J. Cheng, and Z. N. Chen, "Wideband and wide-angle single-layered-substrate linear-to-circular polarization metasurface converter," *IEEE Transactions on Antennas and Propagation*, vol. 68, no. 2, pp. 1186–1191, Feb. 2020, doi: 10.1109/TAP.2019.2938683.

[44] C. H. S. Nkimbeng, H. Wang, D. Yoon, Y. B. Park, H. Han, and I. Park, "Ultra-wideband ultra-thin transmissive linear to circular polarization convertor based on crossed-dipole-shaped metasurface," *IEEE Access*, vol. 12, pp. 120337–120346, 2024, doi: 10.1109/ACCESS.2024.3450707.

[45] C. H. S. Nkimbeng, S. Do, H. Wang, D. Yoon, H. Lee, Y. B. Park, and I. Park, "Miniaturised wideband metasurface polarisation converter with high angular stability," *Scientific Reports*, vol. 16, Art. no. 2797, 2026, doi: 10.1038/s41598-025-32661-z.